Closed Contour Extraction based on Structural Models and Their Likelihood Analysis

Jiayin Liu[1,2] and Yuan Wu[1,3]
[1]DeepSea Precision Tech (Shenzhen) Co., Ltd, B3-4A1 Merchants Guangming Science Park, Shenzhen, Guangdong, China
[2]School of Electronics and Electrical Engineering, Pusan National University, Korea
[3]Digital Media & Systems Research Institute, University of Bradford, U.K.

Keywords: Closed Contour Extraction, Structural Modelling, Likelihood Analysis, Image Processing.

Abstract: In this paper, we describe a new algorithm for extracting closed contours inside images by introducing three basic structural models to describe all potentially closed contour candidates and their likelihood analysis to eliminate pixels of non-closed contours. To further enhance the performance of its closed contour extraction, a post processing method based on edge intensity analysis is also added to the proposed algorithm to reduce the false positives. To illustrate its effectiveness and efficiency, we applied the proposed algorithm to the casting defect detection problem and carried out extensive experiments organized in three phases. The results support that the proposed algorithm outperforms the existing representative techniques in extracting closed contours for a range of images, including artificial images, standard casting defect images from ASTM (American Society for Testing and Materials) and real casting defect images collected directly from industrial lines. Experimental results also illustrate that the proposed algorithm achieve certain level of robustness in casting defect detection under noise environment.

1 INTRODUCTION

Closed contour detection, extraction and analysis remains an important image processing tool for a range of applications, such as object segmentation (Wang et al., 2005; Felzenszwalb and McAllester, 2006), blob analysis (Kawulok, 2010; Diciotti et al., 2010), and shape modelling (Sappa and Vintimilla, 2007; Zhu et al., 2007) etc. Over the past decades, many different algorithms and techniques have been proposed and reported in the published literature within different contexts of applications. Even at present, reliable closed contour extraction still remains an unsolved problem yet its application has significant impact for a number of high-level image content analysis and processing tasks. Representative existing work for closed contour extraction can be summarized as follows.

The general principle for closed contour extraction can be described by two essential steps: (i) detecting all possible closed-contour pixels via edge detection, filtering or any other gradient-based image processing techniques; and (ii) post-processing these detected potential pixels via a range of criteria based approaches, such as modelling, connection and cost measurement etc. to connect them into closed contours. Wang et al exploits the concept of saliency and encoded the Gestalt laws of proximity and continuity to extract closed contours, which achieved good results in extracting closed boundaries for large objects (Wang et al., 2005). By following the similar principle, Sappa and Vintimilla adopted the cost minimization approach to connect the open ended edge points into closed contours (Sappa and Vintimilla, 2007). For small closed-contours, such as blob-like objects and segmented cells etc. filtering and texture analysis based approaches could provide better performances (Kawulok, 2010, Diciotti et al., 2010). Earlier work on contour extraction is based on chain coding technique and object-oriented approaches. These include the algorithm (Pavlidis, 2012; Arbelaez et al., 2011) for contour tracing in binary images, the other similar versions (Ren et al., 2002; Martin et al., 2004) and (Chang et al., 2004), as well as the contour extraction algorithm (Nabout et al., 1995). The inherent weakness of these methods can be summarized as: (i) the need to select appropriate starting points to ensure correct tracing; (ii) the need to determine the appropriate searching direction when the tracing encounters intersections; and (iii)

Liu J. and Wu Y.
Closed Contour Extraction based on Structural Models and Their Likelihood Analysis.
DOI: 10.5220/0006480700400049
In *Proceedings of the 9th International Joint Conference on Knowledge Discovery, Knowledge Engineering and Knowledge Management (KDIR 2017)*, pages 40-49
ISBN: 978-989-758-271-4

limitations to large objects with traceable boundaries.

Active contour was developed in which a so called “Snake” dynamic model is adopted to extract closed contours in gray level images (Kass et al., 1988). Developing flexible processing for different stochastic shapes, a Gradient Vector Flow (GVF) model was further developed which pushes the ‘Snake’ contour into concave regions and provides a relatively free selection of the initial contour position (Xu and Prince, 1998). The active contour techniques work well on a single object with smooth and salient contours in the image. With overlapping of multiple small contours such as cells inside medical images, however, it becomes difficult to get clear, sharp and non-ambiguous contours. Other weaknesses of this method include poor iteration convergence and the need to define the initial contour carefully.

Region growing is another image segmentation method that is also called seed fill or flood-fill method. It takes a set of seed points which are planted within the image to form regions, and the regions are iteratively grown by comparing all unallocated neighbouring pixels to the regions. The difference between the intensity of a pixel and the mean of its region is used as a measure of similarity between pixel and the corresponding region. The pixel with the smallest difference value is allocated to the respective region and it does not stop until all pixels are allocated to the region. An example of application is shown in (Dehmeshki et al., 2008) which intended to extract the closed contours of medical image segmentation. The limitation of this method for practical applications is due to its need to select the seed number and their initial locations, yet such knowledge is often non-available in advance. In addition, the determination of the criteria for the similarity measurement between the seeds and their surrounding regions are sensitive to lighting effect and the variation of differences between the contour region and backgrounds.

In our recent research of developing closed contour extraction algorithms for automatic detection of casting defects on metal casting industrial lines, we have tested all the above representative techniques and found that none of them could provide satisfactory performances. This is primarily due to the fact that: (i) casting defects have a wide range of different appearances, which could either be isolated large closed contours or overlapped multiple blob-like small closed contours; (ii) when captured as images, the difference between the defects areas and their normal background vary significantly, and hence make their performances non-stable without sufficient level of robustness. By following the similar spirit of recent work on closed contour detection in the principle of detecting edges and then connect the selected open-ended edges into closed contours, we have developed a new solution for closed contour extraction, which proves working well in the practical applications of detecting casting defects from X-ray images. The new algorithm can be described in terms of three components: (i) extraction of potential contour points, i.e. detection of all candidates for possible contours; (ii) construction of the closed contours by eliminating non-closed contour candidates, and (iii) further reduction of false positives via a post-processing technique based on edge intensity analysis. In comparison with all the existing technologies, our proposed algorithm makes the following contributions: (i) corresponding to the problem of varying appearances inside the casting defects, the proposed algorithm detects the closed contours in terms of structural models rather than individual pixels through a likelihood analysis scheme; (ii) corresponding to the problem of varying differences between the defects and their background, the proposed algorithm eliminates non-closed contours rather than tracking the closed contours, which are adopted by all the existing methods reported in the literature. Our experimental results support that the proposed algorithm achieves overwhelmingly better performances in comparison with representative existing techniques in terms of both robustness and effectiveness for casting defect detection.

The rest of this paper is organized as follows. Section II describes the proposed algorithm, which includes introduction of basic structural models, likelihood analysis, and the corresponding criteria as well as other relevant strategies introduced. Section III reports the experimental results, which are organized in terms of four phases by running the proposed algorithm on both standard defect images and the real defect images collected from industrial lines. Section IV provides concluding remarks.

2 THE PROPOSED ALGORITHM

While existing work on closed contour extraction follows the principle of detecting potential contour candidates via edge detection or other pixel based processing techniques and then extract the closed contours by further processing these candidates, such as connection of open-ended edges etc. we follow its opposite direction by focusing on eliminating the non-contour candidates, in order to overcome the problem of varying appearances inside the casting defects. Consequently, our proposed algorithm can be described in terms of three operational elements, which include: (i) edge-based detection of contour point candidates; (ii) elimination of non-contour candidates via structural modeling and likelihood analysis; and (iii) false positive reduction via a strategy of dual-thresholding. Details of all the three elements are described as follows.

2.1 Edge-based Detection of Contour Point Candidates

The LoG filter is widely used in a range of image processing technologies (Howlader and Chaubey, 2010), in which its essential operation is to smooth the input image with a Gaussian filter followed by a Laplace operator. A Laplace operator, denoted by ∇^2, is a 2nd derivatives filter which tries to locate the edge points. Its basic idea is that the values of a contour point's neighbors are designated with opposite signs.

Given the input image J with its grey values for a pixel located at the position (i, j) as represented by $J_{i.j}$, F represents the Gaussian filtered image of J by the Gaussian filter with standard deviation σ. R is the LoG filtering output of J, and can be worked out as follows:

$$R_{i,j} = \nabla^2(F) = 4 \times F_{i,j} - [F_{i-1,j} + F_{i+1,j} + F_{i,j-1} + F_{i,j+1}] \tag{1}$$

For the detection of the potential contour points or pixels, we adopt a strategy such that: (i) the detected contour points shall cover all the possible candidates for closed contour extraction; (ii) the detected contour points provide an effective and efficient platform for achieving a high level of robustness in detecting closed contours. Correspondingly, we propose the following condition test:

$$\psi(J_{i,j}) = \begin{cases} 1, & R_{i,j} > 0 \cap \{R_{i-1,j} < 0 \cup R_{i+1,j} < 0 \cup R_{i,j-1} < 0 \cup R_{i,j+1} < 0\} \\ 0, & otherwise \end{cases} \tag{2}$$

Where $\psi(J_{i,j})$ stands for the process of potential contour point detection, and $\psi(J_{i,j}) = 1$ designates that the pixel $J_{i.j}$ is a detected potential contour point or pixel.

The condition test given in (2) is inspired by the basic idea of zero crossing, which is adopted to strengthen the potential contour point detection and thus reduce the risk of the structural modeling at the latter stage. In mathematical terms, a “zero-crossing” is a point where the sign of a function changes (e.g. from positive to negative), represented by a crossing of the axis (zero value) in the graph of the function.

Following such contour point detection, a new binary image I that indicates the positions of those detected potential contour points can be generated by:

$$I_{i,j} = \begin{cases} 1, & \psi(J_{i,j}) = 1 \\ 0, & otherwise \end{cases} \tag{3}$$

By designating that $I_{i,j} = 1$ indicates white color and $I_{i,j} = 0$ black, all pixels inside the binary image can be classified into contour pixels (white) and non-contour pixels (black).

2.2 Structural Modeling

Given the generated binary image, all the detected contour pixels do not necessarily formulate the closed contours. If all pixels which do not belong to any closed contour are removed, all the remaining pixels can be associated with closed contours. This is the essential principle that we adopted for developing the proposed algorithm. Since most of the images are so complicated that the pixels cannot be handled as easily as we described above, we propose to divide the binary image into three basic structural models, and all these three basic models have their own elimination rules, which follow the same principle that the connectivity of the original image should not be changed. In this way, the process of closed contour extraction can be implemented and operated in terms of these basic structural models rather than individual pixels. In other words, by using the proposed structural models, the pixel-to-pixel approach adopted by the existing research can be transformed into a structure-to-structure technique, with which significant advantage can be achieved in the sense that a structure based model provides faster processing speed and better robustness when operating in a noisy environment, as encountered in automatic casting defect detection.

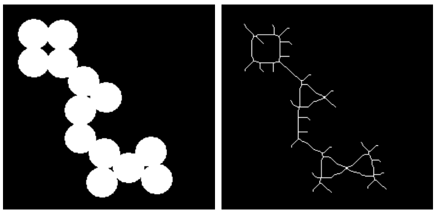
(a) (b)

Figure 1: Illustration of skeleton images: (a) original image I, and (b) the skeleton image S(I).

In order to handle complicated binary images, the original image should be simplified without changing its connectivity. The skeleton of an image is the set of points whose distance from the nearest image boundary is locally a maximum, and skeleton operation can remove pixels on the contours of objects without allowing objects to break apart. From topology theory, it is known that an Euler number is equal to the number of connected components minus the number of holes. As the skeleton operation preserves the Euler number, the connectivity of the original image remains unchanged (Lam et al., 1992). To derive such skeletons, morphological operations can be adopted. Following that, all skeletons extracted can be made to be 1 pixel wide for all the contours, an example of which is shown in Figure 1.

2.3 Basic Structural Models

Given the skeleton of the image $S(I)$, all the directions from each pixel p, to its neighbors can be divided into two categories. One is along the x-axis or y-axis, denoted as direction δ, and the other is the direction that has an angle of 45 degrees to the axis, denoted as direction ξ. As $S(I)$ is a binary image whose contour width is equal to 1, there are at most three pixels ahead if tracking along the contour in one direction. Figure 2 illustrates all the possible situations, where, in the first row, the three blank white circles around pixel p indicate the potential pixel positions that can exist, and in the second, third and last row, there are all the possible situations when p has one, two and three neighbors respectively. The arrows indicate a direction δ, or ξ.

If p is a pixel of $S(I)$, then $N(p)$ is defined as a set that contains all neighboring pixels of p, and $|N(p)|$ is the number of neighboring pixels around p. Let $d(p,q)$ represent the *chessboard* distance between pixels $p(x_p,y_p)$ and $q(x_q,y_q)$, its definition can be described as follows:

$$d(p,q) = \max(|x_p - x_q|, |y_p - y_q|) \qquad (4)$$

Definition 1: C*ompactness* $C(p)$ is a value that indicates how compact in space distribution the neighboring pixels of p are. In general, the smaller the value of *compactness*, the more compact the elements in $N(p)$ are, and thus we have:

$$C(p) = \begin{cases} \dfrac{\sum_{1\leq i<j\leq|N(p)|} d(q_i,q_j)}{C^2_{|N(p)|}}, & |N(p)| \geq 2 \\ 1, & |N(p)| = 1 \end{cases} \qquad (5)$$

When$|N(p) \geq 2|$, $q_1, \cdots, q_{|N(p)|} \in N(p)$,$C^2_{|N(p)|}$is the combinatorial number of selecting 2 items from $|N(p)|$ items. When$|N(p)| = 1$, it means that p has only one neighbor, i.e., the most compact case, and hence $C(p) = 1$.

From the definitions, it can be worked out that: $1 \leq d(q_i,q_j) \leq 2$, and hence $1 \leq C(p) \leq 2$.

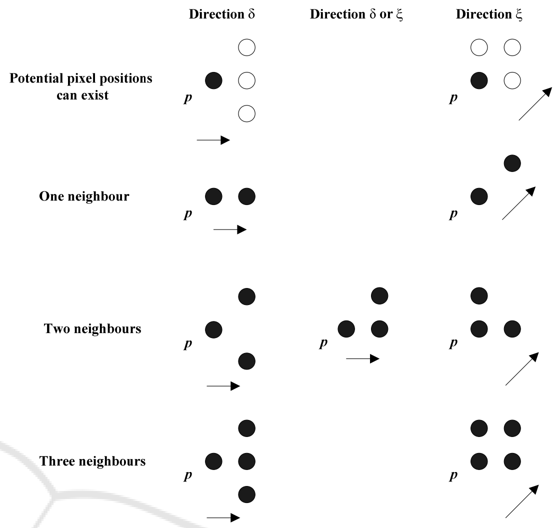

Figure 2: Construction of structural models.

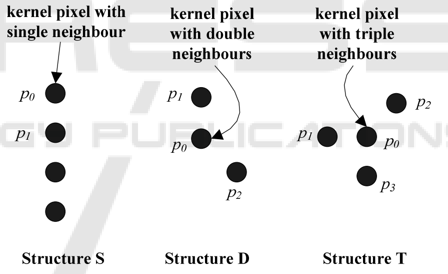
kernel pixel with single neighbour
kernel pixel with double neighbours
kernel pixel with triple neighbours
p0
p1
p2
p3
Structure S
Structure D
Structure T

Figure 3: A schematic drawing of the three basic structures S, D, and T.

Definition 2: A *Structure* is a set of pixels that consists of only one kernel pixel p_0 and several shell pixels $p_1, p_2, \cdots$ which are all neighbors of p_0.

In the proposed algorithm, the principle adopted for the elimination process is that we only remove the kernel pixel p_0 but leave the shell pixels, which are required as evaluation pixels for detecting and removing the kernel pixel.

As a result, depending on the number of neighbors surrounding p_0, we define the three basic structural models as follows, which cover all the situations illustrated in Figure 2. Corresponding to each basic structure, we use a different rule to detect, simplify or remove. A schematic drawing of the three basic structures, *S*, *D*, and *T*, is given in Figure 3.

The definition of the structure S, i.e. the kernel pixel with one *single* neighbor, can be given as follows:

$$S{:}\{p_0, p_1 \mid |N(p_0)| = 1, p_1 \in N(p_0)\} \qquad (6)$$

Where p_0 is a kernel pixel, and p_1 is a shell pixel.
A single pixel p_0 can be treated as a special case inside the Structure $S{:}\{p_0 \mid |N(p_0)| = 0\}$

Structure D (a kernel pixel with *double* neighbors) is defined as:

$$D{:}\{p_0, p_1, p_2 \mid |N(p_0)| = 2, p_1, p_2 \in N(p_0)\} \qquad (7)$$

Where p_0 is a kernel pixel, p_1 and p_2 are shell pixels.

Structure T (a kernel pixel with *triple* neighbors) is defined as:

$$\mathrm{T}{:}\{p_0, p_1, p_2, p_3 \mid |N(p_0)| = 3, p_1, p_2, p_3 \in N(p_0)\} \qquad (8)$$

Where p_0 is a kernel pixel, p_1, p_2 and p_3 are shell pixels.

Each basic structure is required to go through the simplifying or removing process, which primarily aims at removing the kernel pixel, i.e. the non-closed contour candidates. Its removal is dependent on the distribution of its shell pixels. In principle, a structure with a compact distribution of shell pixels means that it has a low probability of changing the connectivity of the remaining shell pixels after the kernel pixel is removed.

A likelihood based elimination scheme is proposed to construct the rule for removing kernel pixels, which is defined as:

$$\Gamma(p) = 2/C(p) - 1 \qquad (9)$$

Where $\Gamma(p)$ is defined as the likelihood value of pixel p, which indicates a priority level that p should be removed as a non-closed contour pixel. The smaller the compactness value $C(p)$ is, the larger the value of $\Gamma(p)$, and hence the higher the priority that p should be removed as a non-closed contour pixel. According to the range of $C(p)$, we have $0 \le \Gamma(p) \le 1$, where $\Gamma(p) = 1$ indicates that p should be removed definitely. Due to noise and other unperceptive factors, not all p pixels that should be removed satisfy the condition $\Gamma(p) = 1$. Correspondingly, we adopt the common principle that, when $\Gamma(p) \ge 0.5$, p is removed, otherwise p stays. Details are described as follows.

For S, we have:$\Gamma(p_0) = 2/C(p_0) - 1 = 1$, and hence p_0 should be removed. This is repeated until nothing is left, this process of which is illustrated in Figure 4.

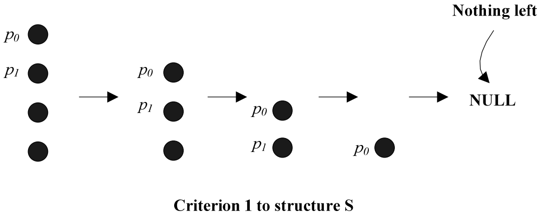

Figure 4: Illustration of a schematic elimination for Structure S.

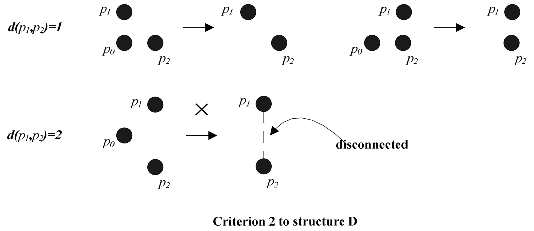

Figure 5: Schematic elimination for Structure D.

For D, we have:

$$C(p_0) = \sum_{1 \le i < j \le 2} d(p_i, p_j)/C_2^2 = d(p_1, p_2).$$

Therefore, removal of p_0 is determined via the likelihood value, which is depending on the value of $d(p_1, p_2)$, as defined below:

$$\Gamma(p_0) = 2/C(p_0) - 1 = \begin{cases} 1, & d(p_1, p_2) = 1 \\ 0, & d(p_1, p_2) = 2 \end{cases} \qquad (10)$$

The removal process is also illustrated in Figure 5, where it is seen that, in the first row when $d(p_1, p_2) = 1$, p_0 can be removed, while in the second row when $d(p_1, p_2) = 2$, p_0 should stay.

For T, we have:

$$\begin{aligned} C(p_0) &= \sum_{1 \le i < j \le 3} d(p_i, p_j)/C_3^2 \\ &= [d(p_1, p_2) + d(p_1, p_3) + d(p_2, p_3)]/3 \end{aligned} \qquad (11)$$

As the value of $C(p_0)$ is dependent on all three distances, specific calculation of the priority level can be derived as follows:

$$\Gamma(p_0) = 2/C(p_0) - 1 = \begin{cases} 1, & d(p_1, p_2) = d(p_1, p_3) = d(p_2, p_3) = 1 \\ 0.5, & d(p_1, p_2) + d(p_1, p_3) + d(p_2, p_3) = 4 \\ 0.2, & d(p_1, p_2) + d(p_1, p_3) + d(p_2, p_3) = 5 \\ 0, & d(p_1, p_2) + d(p_1, p_3) + d(p_2, p_3) = 6 \end{cases} \qquad (12)$$

Similarly, the removal process is illustrated in Figure 6, where, in the first row when $d(p_1, p_2) + d(p_1, p_3) + d(p_2, p_3) = 3$ or $d(p_1, p_2) + d(p_1, p_3) + d(p_2, p_3) = 4$, p_0 can be removed, while in the second row when $d(p_1, p_2) + d(p_1, p_3) + d(p_2, p_3) = 5$ or $d(p_1, p_2) + d(p_1, p_3) + d(p_2, p_3) = 6$, p_0 should stay.

Otherwise p_1 will be separated from p_2 and p_3.

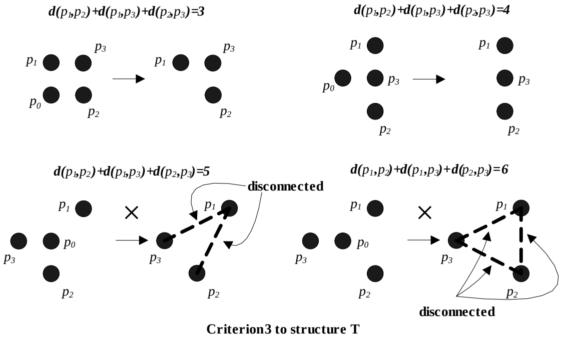
d(p1,p2)+d(p1,p3)+d(p2,p3)=3
p1
p3
p0
p2
d(p1,p2)+d(p1,p3)+d(p2,p3)=4
p1
p0
p3
p2
d(p1,p2)+d(p1,p3)+d(p2,p3)=5
disconnected
p1
p0
p3
p2
d(p1,p2)+d(p1,p3)+d(p2,p3)=6
p1
p0
p3
p2
disconnected
Criterion3 to structure T

Figure 6: Schematic elimination for Structure T.

2.4 False Positive Reduction

To increase the robustness of the proposed scheme in detecting closed-contour candidates, we further propose a validation or post processing scheme to reduce false positives by monitoring and analyzing the differences between the LoG filtered pixels and their surroundings.

Specifically, given an object pixel inside the image, $F_{i,j}$, a value of *MDV* (Maximum Difference Value) is introduced as follows:

$$MDV_{i,j} = \max\{R_{i,j} - R_{i-1,j}, R_{i,j} - R_{i+1,j}, R_{i,j} \\ - R_{i,j-1}, R_{i,j} - R_{i,j+1}\} \quad (13)$$

Where $max\{\}$ represents the maximum value among all the elements inside the bracket, and $R_{i,j}$ represents the LoG filtered pixel.

Since a larger $MDV_{i,j}$ indicates a higher probability that the point $F_{i,j}$ is a contour point, we propose a two-step scheme to reduce the false positives. In the first step, we use a threshold to remove those points where their corresponding *MDV* value is less than a threshold. This is defined below:

$$v(F_{i,j}) = \begin{cases} 1, & MDV_{i,j} > T_1 \\ 0, & else \end{cases} \quad (14)$$

Where $v(F_{i,j})$ represents the validation process, and its value of unity indicates that $F_{i,j}$ is a true positive. Otherwise, $F_{i,j}$ is false positive.

Following the validation process for individual pixels, the second step of our proposed scheme involves an examination of each contour candidate, in which the number of pixels that are labeled as true positives by the first step is counted. This process can be described as follows.

$$v(I_{i,j}) = \begin{cases} 1, & N_o/N_a > T_2 \\ 0, & else \end{cases} \quad (15)$$

Where $v(I_{i,j})$ represents the validation of the contour candidate inside the binary image $I_{i,j}$, N_o stands for the number of pixels labeled as true positives by (14), and N_a stands for the total number of pixels included in the contour candidate being examined.

Determination of the two thresholds is mainly via F-measure caculation approach on ground truth database. The general principle is that the larger the T_1 or T_2 is, the more the false positives are removed. Our extensive empirical studies reveal that T_2 is not particularly sensitive. With T_1, however, it is slightly sensitive to the type of input image.

3 EXPERIMENTS

We formulate closed contour detection as a classification problem of discriminating closed contours from non-contour pixels and apply the precision-recall evaluation framework to benchmark the related algorithms. To evaluate the proposed algorithm, we carried out extensive experiments organized in three phases. The first phase experiments carried out on the ASTM (American Society for Testing and Materials) test data, the second phase experiments carried out on the test data sets with ground truth collected from industrial lines and the final phase is dedicated to robustness analysis, where Gaussian noise is added to the casting defect images and the proposed algorithm is evaluated to see if it can still produce acceptable detection results. PR curve and F-measure are also performed and evaluated, the optimal thresholds of T_1 and T_2 are obtained during the F-measure caculation course.

3.1 Phase-1: Standard Casting Defect Images

According to the suggestions made by ASTM (American Society for Testing and Materials), all standard casting defect images are divided into seven categories in terms of the type of defects, which include: air holes, foreign-object inclusions (slag and sand), shrinkage cavities, cracks, wrinkles, casting fins, and abnormal micro-fracture. Figure 7 illustrates samples of all seven categories.

In Li's paper (Li et al., 2006), the algorithm is only tested on ASTM standard images. It should be noticed that the ASTM standard images are not designed for quantity evaluation, thus our results compared with Li's do not give quantity evaluation further. From the illustrated results in Figure 8, it is cleared that our method outperforms Li's especially in details of the segmented defects. (To facilitate the comparison with Li's result, we inverted the gray values of our result images.)

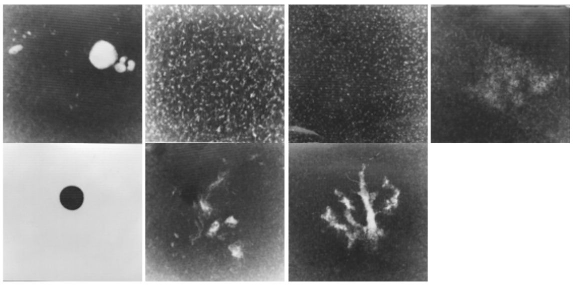

Figure 7: Representative samples of the seven categories of casting defects.

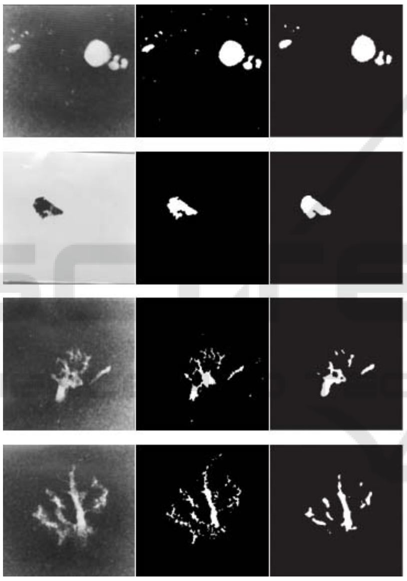

Figure 8: Illustration of comparative experiments between the proposed and Li's work: from the leftmost to the rightmost, the three columns are the original ASTM standard images, our results, Li's results.

While Li's work did not report any of their testing results on real defect images, the proposed algorithm works well with processing real defect images as reported in phase-2 of our experiments.

3.2 Phase-2: Real Defect Images and Ground Truth

In this phase, we applied the proposed algorithm to a range of real casting defect images collected from industrial line and tested its usefulness in practical applications and performance based on ground truth. The ground truth datasets have two forms: the contour form that can be tested by contour-based methods, and the region form that will be used by region-based methods such as thresholding techniques. Basically, the two forms are equal: the region form ground-truth is labelled by three different professional examiners by hand-drawn, at least two hints on one pixel will make this pixel labelled as an object from the background in the ground-truth; the contour form ground-truth is the closed contours of the region form ground-truth. The ground truth datasets contain 3080 positive samples and 8600 negative samples.

A sample image and its detailed processing results are illustrated in Figure 9.

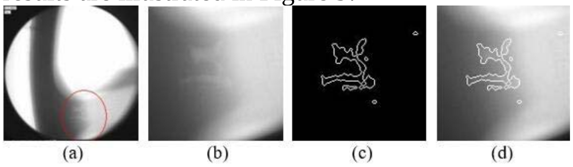

Figure 9: Sample experimental results by the proposed: (a) The original image captured from an industrial line, where the defects are labeled in the circle; (b) illustration of the defect via zooming-in of the original image; (c) Closed contour extracted by the proposed; (d) Superimposed contours with the defects on the original image.

We formulate closed contour detection as a classification problem of discriminating closed contours from non-contour pixels and apply the precision-recall evaluation framework to benchmark the related algorithms, including Mery's (Mery and Filbert, 2002), Li's (Li et al., 2006), Canny (Canny, 1986), and some recently published works to the best of our knowledge (Zhao et al., 2014; Zhao et al., 2015; Ramírez and Allende, 2013). The ground truth data set contains 5,000 X-ray images collected from the real industrial environment. Mery's performed better than others. We will perform comparative tests between Mery's and our method thoroughly.

Some samples from the ground truth and their corresponding results are presented in Figure 10: from the leftmost column to the rightmost, they are the original images, contour form ground truth,
region form ground truth, our results, Canny's results, Mery's results (Mery and _Filbert, 2002), Elder's (Elder and Zucker, 1998).

The preferred evaluation measure the precision recall (PR) framework can capture the trade-off between accuracy and noise while the algorithm threshold varies. Using the PR evaluation is a standard evaluation technique in information retrieval, *precision* is the fraction of retrieved instances that are relevant, $precision = tp/(tp + fp)$, while *recall* is the fraction of relevant instances that are retrieved, $recall = tp/(tp + fn)$. Receiver operating characteristic (ROC) curves are considered not appropriate for quantifying boundary or contour detection in classification tasks (Martin et al., 2004). In our work, the *precision* is the number of true positives (i.e. the number of pixels correctly labelled as belonging to the positive class) divided by the total number of pixels labelled as belonging to the positive class (i.e. the sum of true positives and false positives), and *recall* is defined as the number of true positives divided by the total number of elements that actually belong to the positive class (i.e. the sum of true positives and false negatives).

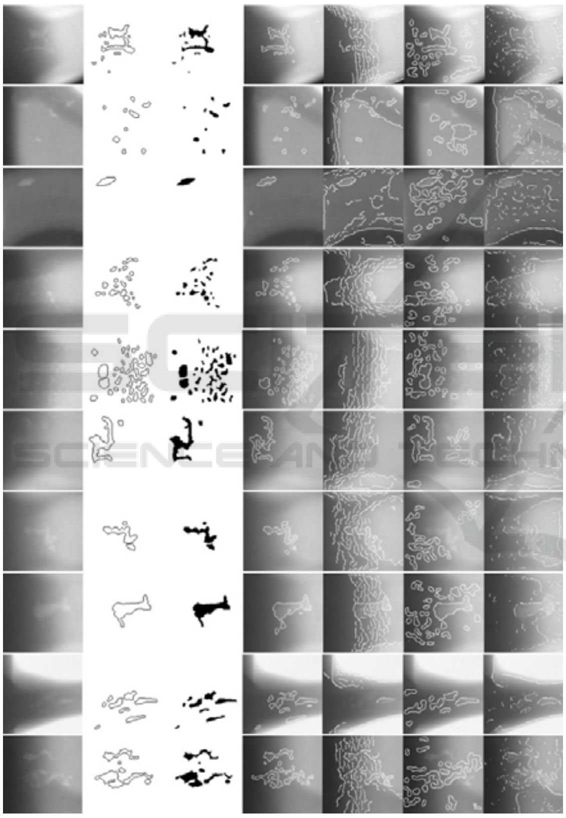

Figure 10: Illustration of ground truth and their corresponding results: From the leftmost column to the rightmost, they are original images, contour form ground truth, region form ground truth, our results, Canny's, Mery's and Elder's results.

Usually, precision and recall scores are not discussed in isolation. Instead, either value for one measure is compared for a fixed level at the other measure. A measure that combines precision and recall is the harmonic mean of precision and recall, the traditional F-measure:

$$F = \frac{2 \cdot precision \cdot recall}{precision + recall} \tag{16}$$

This is also known as the F_1 measure, because *recall* and *precision* are evenly weighted. PR curves based on threshold T_1 and T_2 are illustrated in Figure 11, in which we alter T_1 from 0 to 0.6, and T_2 from 0 to 0.8.

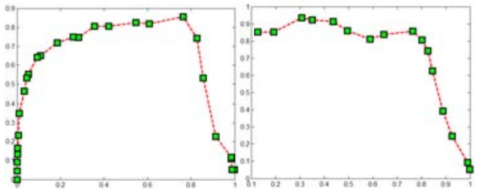

(a) (b)

Figure 11: PR curves based on threshold T_1 and T_2, in which the horizontal axis is recall, and the vertical axis is precision, left: $T_1$from 0 to 0.6, right: $T_2$from 0 to 0.8.

The location of the maximum *F*-measure along the PR curve provides the optimal algorithm threshold. In table 1, we could see the optimal thresholds ($T_1 = 0.16$ and $T_1 = 0.35$) are obtained during the *F*-measure caculation course.

Table 1: The optimal thresholds obtained based on F-measure.

Method	Our algorithm (T_1)	Our algorithm (T_2)
F-measure @parameter	$0.78@T_1 = 0.14$ $\mathbf{0.79@T_1 = 0.16}$ $0.68@T_1 = 0.18$	$\mathbf{0.797@T_2 = 0.35}$ $0.793@T_2 = 0.4$ $0.75@T_2 = 0.45$

We carried out further experiments for performance comparison between Mery's and ours, the PR curve is presented in Figure 12. From the illustrations in Figure 10 and the PR curve performance in Figure 12, it shows that the proposed method performs better.

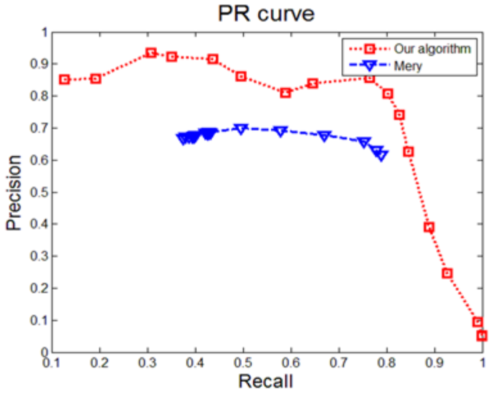

Figure 12: The proposed algorithm and Mery's performance are evaluated with PR curves.

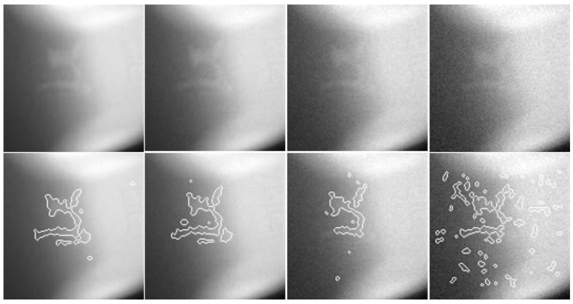

Figure 13: Experimental results to test the robustness of the proposed algorithm, the top row, from left to right: The original image, corrupted images with additive Gaussian noise of variances 1, 2, 3 respectively, the bottom row, from left to right: The corresponding results, superimposed closed contours with the real defects inside the original images.

3.3 Phase-3: Robustness Test and Computing Burden

To test the robustness of the proposed algorithm, we added Gaussian noise to the X-ray images with three levels of variance and repeated the experiments. Figure 13 illustrates a sample of such test results, in which the original image and its corrupted versions with variances of 1, 2 and 3 are shown from left to right on the top row, and the results are shown in the bottom rows. As seen, the proposed algorithm is able to produce acceptable detection results with a noisy environment until the variance level is increased to 3. This result illustrates a high level of robustness achieved by the proposed algorithm, although, for the case of noisy environment with variance of 3, the proposed algorithm failed to achieve right detection of the closed contours. This is reasonable due to the fact that, under this circumstance, it is difficult to see the real defect even with our naked eyes as shown in the right-most column. It should also be noted that, during the entire experiments, no extra de-noise technique has been applied to the proposed algorithm.

On a PC with Intel Core i7-2600 3.4GHz CPU and 8GB RAM, the average processing time of our method in MATLAB implementation is around 0.45 seconds per image. The image resolution is 140*140 pixels.

4 CONCLUSIONS

In this paper, we described a structural model based approach for closed contour detection, which is prompted by our recent research on developing image-based algorithms for casting defect detection. In comparison with the existing techniques, the proposed algorithm has the following features: (i) closed contour detection and extraction is carried out in terms of structural models rather than individual pixels; (ii) removal of non-closed contour candidates is guided via likelihood analysis. Extensive experiments were carried out to evaluate the proposed algorithm, and all the results show that the proposed algorithm is capable of achieving excellent results for closed contour detections, providing a robust tool for casting defect detection in practical applications.

REFERENCES

Wang, S., Kubota, T., Siskind, J. M., & Wang, J. 2005. Salient closed boundary extraction with ratio contour. *IEEE transactions on pattern analysis and machine intelligence*, 27(4), 546-561.

Kawulok, M. 2010. Energy-based blob analysis for improving precision of skin segmentation. *Multimedia Tools and Applications*, 49(3), 463-481.

Diciotti, S., Lombardo, S., Coppini, G., Grassi, L., Falchini, M., & Mascalchi, M. 2010. The LoG Characteristic Scale: A Consistent Measurement of Lung Nodule Size in CT Imaging. *IEEE transactions on medical imaging*, 29(2), 397-409.

Sappa, A. D., & Vintimilla, B. X. 2007. Cost-based closed-contour representations. *Journal of Electronic Imaging*, 16(2), 023009-023009.

Pavlidis, T. 2012. Algorithms for graphics and image processing. *Springer Science & Business Media*.

Ren, M., Yang, J., & Sun, H. 2002. Tracing boundary contours in a binary image. *Image and vision computing*, 20(2), 125-131.

Chang, F., Chen, C. J., & Lu, C. J. 2004. A linear-time component-labeling algorithm using contour tracing technique. *Computer Vision and Image Understanding*, 93(2), 206-220.

Nabout, A., Su, B., & Eldin, H. 1995. A novel closed contour extractor, principle and algorithm. In *Circuits and Systems, 1995. ISCAS'95., 1995 IEEE International Symposium on* (Vol. 1, pp. 445-448). IEEE.

Kass, M., Witkin, A., & Terzopoulos, D. 1988. Snakes: Active contour models. *International journal of computer vision*, 1(4), 321-331.

Xu, C., & Prince, J. L. 1998. Snakes, shapes, and gradient vector flow. *IEEE Transactions on image processing*, 7(3), 359-369.

Elder, J. H., & Zucker, S. W. 1998. Local scale control for edge detection and blur estimation. *IEEE Transactions on Pattern Analysis and machine intelligence*, 20(7), 699-716.

Dehmeshki, J., Amin, H., Valdivieso, M., & Ye, X. 2008. Segmentation of pulmonary nodules in thoracic CT scans: a region growing approach. *IEEE transactions on medical imaging*, 27(4), 467-480.

Howlader, T., & Chaubey, Y. P. 2010. Noise reduction of cDNA microarray images using complex wavelets. *IEEE transactions on Image Processing*, 19(8), 1953-1967.

Lam, L., Lee, S. W., & Suen, C. Y. 1992. Thinning methodologies-a comprehensive survey. *IEEE Transactions on pattern analysis and machine intelligence*, 14(9), 869-885.

Mery, D., & Filbert, D. 2002. Automated flaw detection in aluminum castings based on the tracking of potential defects in a radioscopic image sequence. *IEEE Transactions on Robotics and Automation*, 18(6), 890-901.

Mery, D., da Silva, R. R., Calôba, L. P., & Rebello, J. M. 2003. Pattern recognition in the automatic inspection of aluminium castings. *Insight-Non-Destructive Testing and Condition Monitoring*, 45(7), 475-483.

Li, X., Tso, S. K., Guan, X. P., & Huang, Q. 2006. Improving automatic detection of defects in castings by applying wavelet technique. *IEEE Transactions on Industrial Electronics*, 53(6), 1927-1934.

Canny, J. 1986. A computational approach to edge detection. *IEEE Transactions on pattern analysis and machine intelligence*, (6), 679-698.

Felzenszwalb, P., & McAllester, D. 2006. A min-cover approach for finding salient curves. In *Computer Vision and Pattern Recognition Workshop, 2006. CVPRW'06. Conference on* (pp. 185-185). IEEE.

Zhu, Q., Song, G., & Shi, J. 2007. Untangling cycles for contour grouping. In *Computer Vision, 2007*. ICCV 2007. IEEE 11th International Conference on (pp. 1-8). IEEE.

Martin, D. R., Fowlkes, C. C., & Malik, J. 2004. Learning to detect natural image boundaries using local brightness, color, and texture cues. *IEEE transactions on pattern analysis and machine intelligence*, 26(5), 530-549.

Arbelaez, P., Maire, M., Fowlkes, C., & Malik, J. 2011. Contour detection and hierarchical image segmentation. *IEEE transactions on pattern analysis and machine intelligence*, 33(5), 898-916.

Zhao, X., He, Z., & Zhang, S. 2014. Defect detection of castings in radiography images using a robust statistical feature. *JOSA A*, 31(1), 196-205.

Ramírez, F., & Allende, H. 2013. Detection of flaws in aluminium castings: a comparative study between generative and discriminant approaches. *Insight-Non-Destructive Testing and Condition Monitoring*, 55(7), 366-371.

Zhao, X., He, Z., Zhang, S., & Liang, D. 2015. A sparse-representation-based robust inspection system for hidden defects classification in casting components. *Neurocomputing*, 153, 1-10.